Journal of Materials Chemistry B

ROYAL SOCIETY OF CHEMISTRY

PAPER

View Article Online
View Journal | View Issue

Cite this: J. Mater. Chem. B, 2023, 11, 1090

Pt(II) metallacycles encapsulated by ferritin enable precise cancer combination chemo-photodynamic therapy†

Xuehong Min‡,[a] Ming Li‡,[c] Wenjing Zhang‡,[c] Run-Hao Li,[b] Zhe Zhang,[d] Pingshan Wang,[d] Weide Su,[c] Feng Li,*[c] Yue Sun *[b] and Yi Liu *[b]

Different from common anti-tumor drugs, organoplatinum(II) metallacycles can integrate imaging and other therapeutic capabilities by incorporating corresponding functional donor ligands to enable potential applications in biomedicine. However, most of the emerging therapeutic agents not only show poor solubility and selectivity but also have serious side effects and unsatisfactory efficacy and encounter the tendency to develop drug resistance due to their single treatment model. Herein, an organoplatinum(II) metallacycle (PtM) was designed and synthesized using coordination-driven self-assembly *via* the combination of a metallic chemotherapy precursor and a reactive oxygen species generating organic precursor. The hydrophobic PtM molecules were encapsulated in the cavity of human heavy chain ferritin (HFn) during the reassembly of HFn to prepare the active targeting nanoagent HFn-PtM for use in chemo-photodynamic combination therapy. The HFn-PtM nanoagents exhibited excellent stability in buffer (pH from 5 to 7.2), alleviating the concern of drug leakage during circulation. A cellular uptake assay indicated that HFn-PtM could efficiently enter specific cells that overexpress the transferrin receptor 1. *In vitro* and *in vivo* anti-tumor investigations revealed that HFn-PtM exhibited excellent anti-tumor efficiency with negligible systemic toxicity. This work provides a strategy for the easy construction of multifunctional organoplatinum-based tumor-targeted drugs.

Received 28th October 2022,
Accepted 10th December 2022

DOI: 10.1039/d2tb02349k

rsc.li/materials-b

1. Introduction

In recent decades, great progress has been made in the development of supramolecular coordination complexes (SCCs) for use in many fields and especially for biomedical applications.[1–6] As a classic type of SCC, the Pt(II) metallacycle has attracted particular attention for the chemotherapeutic treatment of cancer.[7–10] More interestingly, multi-functionalized Pt(II) metallacycles combined with phototherapy have been developed to enhance the effect of tumor treatment, which allows the incorporation of functional groups through post-self-assembly modifications.[11–13] Compared with clinical platinum-based drugs (oxaliplatin, carboplatin and cisplatin), discrete Pt(II) metallacycle-encapsulated nano-agents exhibit low systemic toxicity and a good anti-tumor effect. To date, Pt(II) metallacycle nanodots are mainly formed by encapsulation of polymers and self-assembly of chemically modified water-soluble groups.[14–16] For example, Zhou *et al* designed a supramolecular block copolymer Pt-PBEMA-*b*-POEGMA, which could self-assemble into a nanomedicine, exhibiting effective antitumor activity.[17] In addition, the targeting of Pt-based SCCs is mostly by passive targeting at present.[18–20] Compared with passive targeted nanosystems, active targeting can considerably increase the quantity of drug delivered to target cells, thereby improving the treatment efficiency and limiting the side effects.[21,22] In other word, the preparation of multiple functionalized Pt(II) metallacycle nanoparticles with excellent biocompatibility, active targeting, good stability and effective therapeutic effect is still highly desirable.

Inspired by the intrinsic multifunctionality of human heavy chain ferritin (HFn) in nature, HFn is composed of 24 units that self-assemble into a nanocage with inner and outer dimensions of 8 and 12 nm, respectively, and is easily prepared in large quantities by biosynthesis.[23] HFn has emerged as a novel type of biological nanoparticle for use in imaging and drug delivery platforms for the treatment of cancer.[24–27] In addition, HFn has been found to bind specifically to the transferrin receptor 1

[a] Wuhan Business University, Wuhan 430056, P. R. China
[b] Key State Key Laboratory of Separation Membrane and Membrane Process & Tianjin Key Laboratory of Green Chemical Technology and Process Engineering, School of Chemistry, Tiangong University, Tianjin 300387, P. R. China
[c] State Key Laboratory of Virology, Wuhan Institute of Virology, Center for Biosafety Mega-Science, Chinese Academy of Sciences (CAS), Wuhan 430071, P. R. China
[d] Institute of Environmental Research at Greater Bay Area, Key Laboratory for Water Quality and Conservation of the Pearl River Delta, Ministry of Education, Guangzhou University, Guangzhou 510006, P. R. China

† Electronic supplementary information (ESI) available. See DOI: https://doi.org/10.1039/d2tb02349k

‡ Xuehong Min, Ming Li and Wenjing Zhang contributed equally to this work.

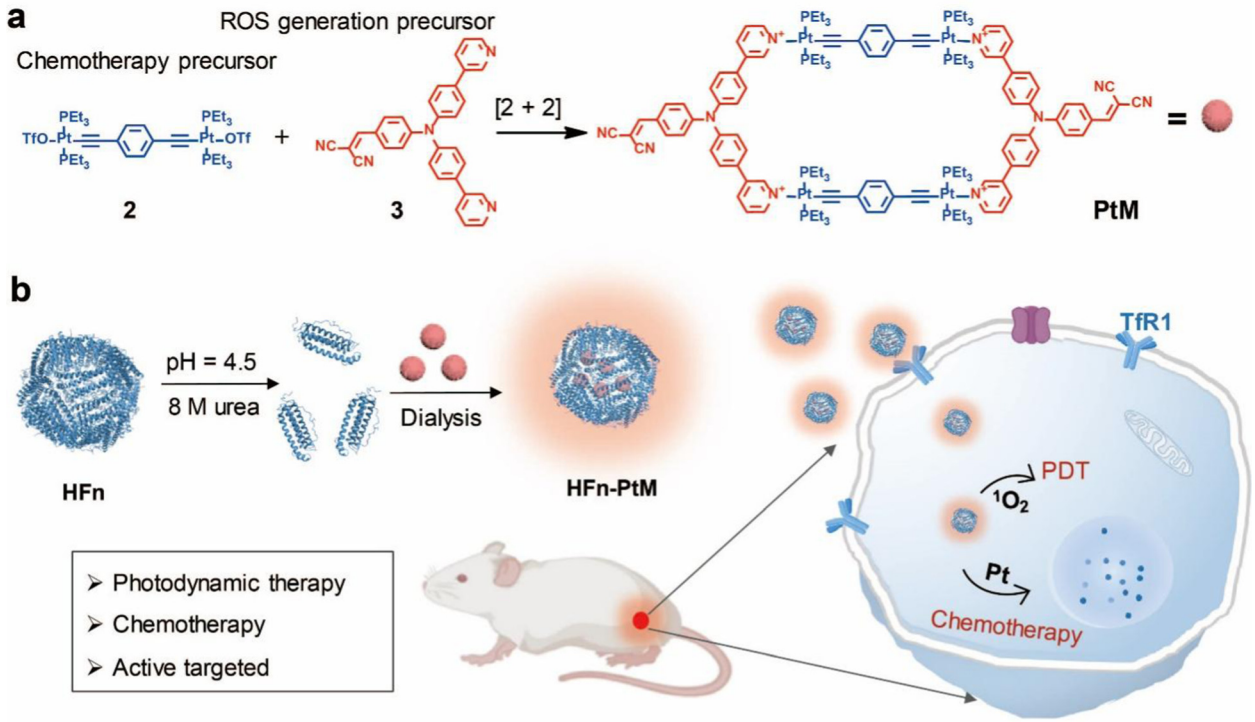

Scheme 1 (a) Schematic of the synthesis of an organoplatinum(II) metallacycle PtM. (b) Schematic illustration of the preparation of the HFn-PtM targeted chemo-photodynamic combination therapy after intravenous (i.v.) injection under light irradiation.

(TfR1), which is overexpressed on tumor cells, including breast, colon and prostate cancer cells.[28] Photodynamic therapy (PDT) is an important emerging method for cancer treatment because of its ability to be accurately controlled, non-invasiveness, lack of side effects, and negligible drug resistance.[29–34] PDT combined with chemotherapy has been proven to be effective in improving treatment efficiency, which can reduce drug resistance.[35–38]

Herein, we successfully synthesized a Pt(II) metallacycle (named PtM) *via* coordination-driven self-assembly, combining the dicyanovinyl group for effectively generating reactive oxygen species (ROS) with the 180° Pt(II) building block for an anticancer drug. In addition, we readily prepared the high biocompatibility nanoagent (HFn-PtM) that integrates photodynamic therapy, chemotherapy, imaging and active targeting by a simple and easy-to-operate method (Scheme 1). *In vitro* experiments indicate that the HFn-PtM has good photodynamic properties and high cancer cell mortality. In mice models, the HFn-PtM shows a chemo-photodynamic combination antitumor effect with negligible systemic toxicity. We expect that this study may provide an approach for easily preparing multifunctional SCC-based targeted drugs with great biocompatibility.

2. Experimental

2.1 Materials and instruments

All chemicals were commercially available and used without further purification. Deionized water (18.2 MΩ cm^{-1}) used in all experiments was purified using a Millipore filtration system (Millipore Corporation, Bedford, USA). All nuclear magnetic resonance spectroscopy (NMR) spectra were recorded on a Bruker AVANCE III at 400 MHz. High-resolution mass spectrometry experiments were carried out using a Micromass Quattro II triple-quadrupole mass spectrometer with electrospray ionization and analyzed with the MassLynx software suite. The UV-Vis spectra were recorded using a spectrophotometer (UV-3600, Shimadzu, Japan) in a quartz cuvette. The fluorescence experiments were carried out using a Cary Eclipse Fluorescence Spectrophotometer (Agilent Technologies).

2.2 Fabrication of the metallacycle PtM

180° Pt(II) precursor **2** (100 mg, 0.078 mM) and 120° precursor **3** (37 mg, 0.078 mM) were placed in a vial, followed by the addition of methanol (3.2 mL). After reacting at room temperature for 8 h, the PtM was obtained by precipitation with diethyl ether (128 mg, 94%). ^{1}H NMR (600 MHz, DMSO-d_6, 295 K): 8.98 (s, 4H), 8.80 (d, J = 4.7 Hz, 4H), 8.44 (t, J = 8.2 Hz, 4H), 8.35 (d, J = 13.7 Hz, 4H), 7.96–7.88 (m, 8H), 7.82 (dd, J = 13.5, 5.4 Hz, 8H), 7.44 (t, J = 8.1 Hz, 8H), 7.15 (s, 8H), 5.76 (s, 2H), 1.84–1.75 (m, 48H), 1.13–1.07 (m, 72H). ^{31}P{^{1}H} NMR (DMSO-d_6, room temperature, 121.4 MHz). δ (ppm): 15.37 ppm (s, ^{195}Pt satellites, $^1J_{Pt-P}$ = 2289.6 Hz). ESI-TOF-MS: m/z 731.25 $[M - 4OTf]^{4+}$, 1014.66 $[M - 3OTf]^{3+}$, 1611.49 $[M - 2OTf]^{2+}$.

2.3 Expression and purification of HFn

HFn was successfully inserted into the plasmid pET28a, and then, it was transformed into Escherichia coli BL21 (DE3), and the cells were induced by isopropyl β-D-1-thiogalactopyranoside (IPTG) in a lysogeny broth (LB) culture medium at 25 °C for 10 h

and broken using a high-pressure homogenizer (AH-1500, ATS Engineering Ltd) in the phosphate-buffered saline (PBS, pH = 7.2). The supernatant harvested by centrifugation at 10 000 rpm for 30 min was filtered through a 0.22 μm filter (Millipore) and heated in a water bath at 60 °C for 15 min, then the supernatant was collected by centrifugation at 10 000 rpm for 30 min and then centrifuged using an ultracentrifuge (Beckman Coulter) at 55 000 rpm (rotor: Ty70) for 2 h; finally, the precipitant was re-dispersed in PBS.

2.4 Preparation of the HFn-PtM

The loading of PtM into the cage of HFn was prepared with the process of disassembly and reassembly of protein nanocages. HFn at 2.0 mg mL^{-1} was dialyzed against in PBS at pH 5.0 with 8 M urea and gently stirred for 12 h at room temperature to ensure complete dissociation of HFn. First, the concentration of disassembled HFn was diluted to 1.0 mg mL^{-1} using PBS containing 20% dimethyl sulfoxide. Then, 10 fold (PtM : HFn cage = 10 : 1) PtM solution was dropped into the solution and the mixture was incubated for 30 min in darkness, the mixture was transferred into dialysis bags (MWCO 3500 Da, Thermo Scientific) and dialyzed against gradient concentrations of urea buffer (4, 2, and 0 M) at 4 °C to slowly reassemble HFn nanocages. After HFn refolding, the solution was centrifuged at 10 000 rpm for 10 min to obtain the precipitate and re-dispersed in PBS.

2.5 Confocal laser scanning microscopy imaging studies

Confocal fluorescence imaging was performed using a Nikon A1 confocal laser-scanning microscope (Tokyo, Japan) with a 60× glycerol immersion objective. On the night before the imaging experiments, all cells were seeded on 35 mm Petri dishes with 20 mm bottom wells (1×10^5 per well). On the following day, the cells were treated with 10 μM HFn-PtM for approximately 4.0 h at 37 °C under a 5% CO_2 atmosphere. Then, the cells were washed with PBS three times and a certain amount of PBS was added. The cells were subject to imaging analysis.

2.6 *In vitro* cytotoxicity evaluation

The cytotoxicity of the HFn-PtM nanoagent against MCF-7 cells was determined by CCK-8 in a 96-well cell culture plate. The cells were seeded at a density of 5000 cells per well in a 96-well plate in the culture media and incubated for 24 h for attachment. The cells were then incubated with fresh serum-supplemented culture media with the HFn-PtM at various concentrations as experiment groups and the cells were incubated with only fresh serum-supplemented culture media as blank control groups. For the groups with irradiation, each well was exposed to white light irradiation (200 mW cm^{-2}, 10 min), while other cells were incubated in the dark. The incubation continued for an additional 24 h. Lastly, the cells were added to the CCK-8 reagent with a measured optical density of 450 nm to evaluate cell viability.

2.7 *In vivo* antitumor activity

Five-week-old female BALB/c mice, with an average weight of 20 ± 2 g, were purchased from Weitong Lihua Experimental Animal Technology Co. Ltd (Beijing, China) and housed in a pathogen-free animal facility. All the protocols for the animal tests have been reviewed and approved by the Committee on Animals at Hubei province and performed in accordance with the guidelines provided by the National Institute of Animal Care. The mice were randomly divided into three treatment groups, and the average tumor volume was about 100 mm^3. The mice were injected intravenously with PBS (100 μL), HFn-PtM (100 μL), and HFn-PtM (100 μL), and mice of group 3 were treated with white light irradiation (200 mW cm^{-2}) for 10 min after the HFn-PtM were injected for 24 h. Five days later, both intravenous injection and light irradiation treatment were repeated. Body weight and tumor volume were measured every 2 days. Tumor volume (mm^3) was calculated as $(\text{width})^2 \times (\text{length}) \times 1/2$. The tumor inhibition study was stopped on the 15th day and the excised tumors were photographed and weighed. Major organs including the heart, liver, spleen, lungs, and kidneys as well as the tumors were harvested for an imaging study and then fixed overnight in 4% paraformaldehyde, embedded in paraffin, cut into 4 μm sections, and mounted onto glass slides. After being stained with H&E, we observed the pathological changes under an optical microscope (3DHISTECH Pannoramic MID).

3. Results and discussion

The discrete metallacycle PtM containing 180° Pt(II) precursor **2** and 120° precursor **3** was synthesized *via* the coordination driven self-assembly as shown in Scheme 1a.[39] The organoplatinum(II) ligands in PtM are for cancer chemotherapy, while the dicyanovinyl group in PtM can efficiently generate ROS by reacting with biological thiol molecules under light irradiation.[40] The precursor **3** was synthesized according to the reported reference and was characterized by ^1H and ^{13}C NMR (Fig. S1–S3, ESI†).[41] The structure of the PtM was characterized by multinuclear NMR analysis (Fig. S4, ESI†). The $^{31}P\{^1H\}$ NMR spectrum of PtM showed a singlet peak at *ca.* 15.37 ppm along with concomitant ^{195}Pt satellites. (Fig. S5, ESI†). Moreover, we observed three peaks at m/z = 731.25, 1024.66, and 1611.49 in the ESI-TOF-MS spectra, corresponding to different charge states $[PtM - 4OTf]^{4+}$, $[PtM - 3OTf]^{3+}$, and $[PtM - 2OTf]^{2+}$ species, respectively (Fig. 1b and Fig. S6, ESI†). These peaks can match well with the calculated theoretical distributions, thus providing further evidence for the formation of discrete PtM. The optimized structure of PtM was calculated by molecular stimulation using the B3LYP/LANL2DZ basis. It possessed a well-defined hexagon with a length of *ca.* 4.7 nm and width of *ca.* 2.4 nm (Fig. 1a). The ultraviolet-visible absorption spectra and fluorescence spectra of PtM were acquired in tetrahydrofuran (THF), 1.2-dichloroethane (DCE), acetonitrile, and dimethyl sulfoxide (DMSO) (Fig. 1c and d). The fluorescence intensities of PtM decreased with increasing polarity of the organic solvent, because of the twisted intramolecular charge-transfer in strong polar solvents. HFn was expressed in *Escherichia coli* and purified by precipitation with ammonium sulfate

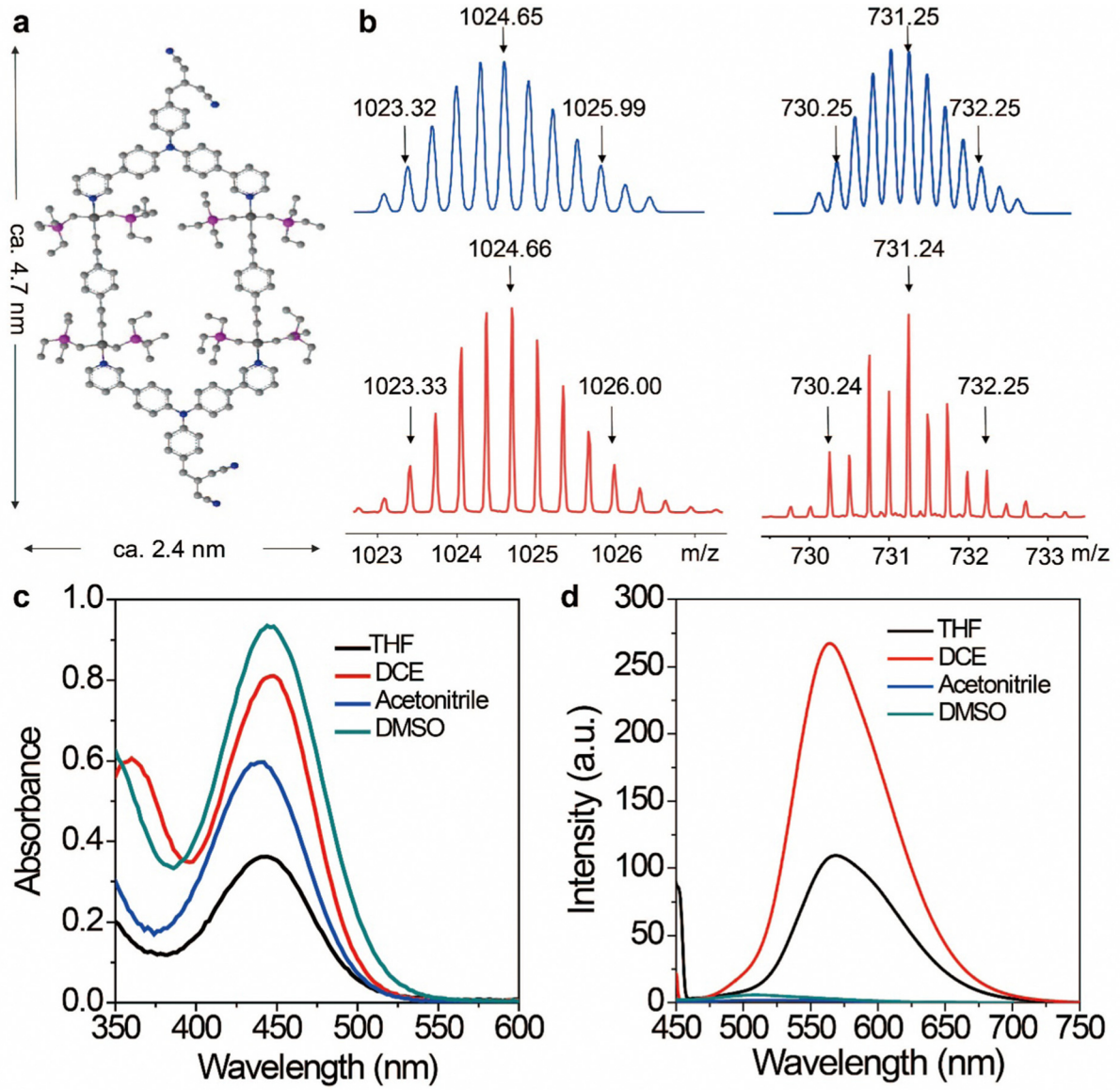

Fig. 1 Molecular calculation and characterization of molecular properties. (a) The optimized structure for metallacycle PtM using B3LYP/LANL2DZ. (b) ESI-TOF-MS spectra of PtM. We observed three peaks at m/z = 731.25 and 1024.66 in the ESI-TOF-MS spectrum, corresponding to different charge states $[PtM - 4OTf]^{4+}$ and $[PtM - 3OTf]^{3+}$ species, respectively. The inset shows experimental (red) and calculated (blue) results. (c) UV-Vis absorption spectra and (d) fluorescence emission spectra of 20 μM PtM in THF, DCE, acetonitrile, and DMSO, respectively.

as previously described.[42,43] HFn-PtMs were achieved by loading PtM into the cavities of HFn nanocages through disassembling HFn in 8 M urea at pH 5.0 (Fig. S7, ESI†). PtM dissolved in DMSO was added under gentle stirring to the disassembled HFn. The ferritin cage was reassembled together with PtM by a reassembling process with a series of stepwise gradients of urea concentrations from 8 M to 0 M in PBS. Finally, the HFn-PtM was obtained by gradient centrifugation (Fig. S8, ESI†). The X-ray photoelectron spectroscopy results indicated that HFn-PtM contained Pt and P elements (Fig. S9, ESI†). The fluorescence spectra of the HFn-PtM ranged from 550 to 800 nm with an emission peak at 600 nm. The UV/Vis absorption spectra analysis showed that HFn-PtM exhibited the characteristic absorption of PtM at 450 nm (Fig. 2d). The PtM content in the HFn-PtM was quantitated by the specific absorbance of PtM at 450 nm in a HFn solution (Fig. S10, ESI†), and the HFn protein content was determined by sodium dodecyl sulfate polyacrylamide gel electrophoresis (SDS-PAGE)/densitometry (Fig. S11, ESI†). We found that the number of PtM molecules (26 PtM molecules) packed in each HFn nanocage was less than that of DOX molecules,[44] possibly due to the relatively large size of PtM molecules (Fig. 1a). The HFn-PtM showed a well-defined spherical morphology determined by transmission electron microscopy (TEM) (Fig. 2a). Moreover, dynamic light scattering (DLS) analysis showed that the hydrodynamic size of HFn-PtM in PBS was *ca.* 13.32 nm and the inset shows that HFn-PtMs were monodispersed in solution (Fig. 2b), suggesting good water solubility and stability of the HFn-PtM. The ζ-potential

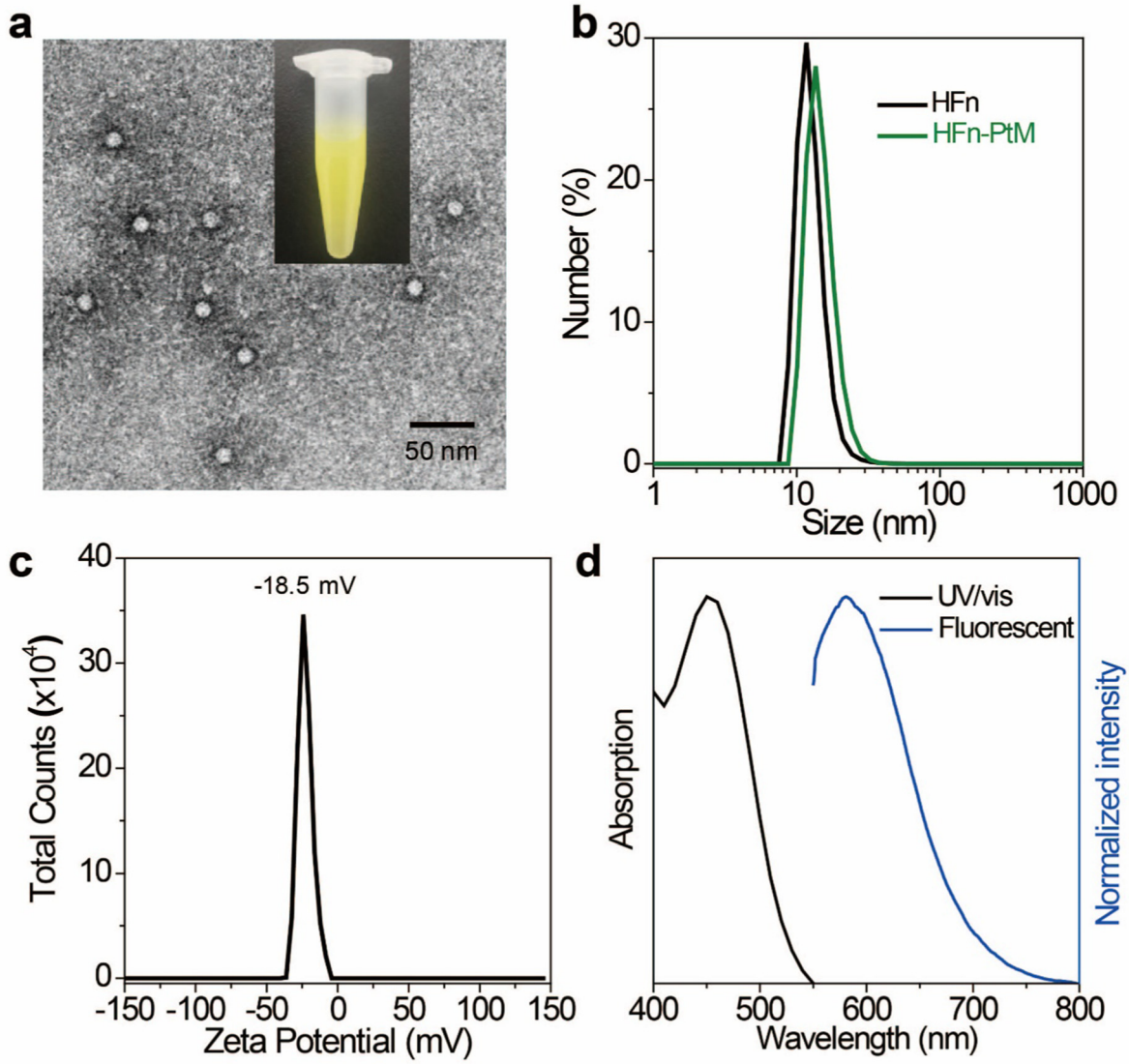

Fig. 2 Characterization of the HFn-PtM. (a) TEM image of the HFn-PtM in PBS, The inset shows images of HFn-PtM in the aqueous solution. (b) DLS measurements of the HFn-PtM and HFn in PBS. (c) Zeta potential (−18.5 mV) of the HFn-PtM. (d) UV-Vis absorption (black) and fluorescence spectra (blue) of the HFn-PtM in PBS.

distribution of the HFn-PtM was −18.5 mV (Fig. 2c). To further investigate the formation process of HFn-PtMs, we conducted molecular docking simulation using the precursor **3** with Discovery Studio 2019 software. This result demonstrated that the precursor **3** was bound to a specific pocket of HFn monomers with an affinity of −34.911 kcal mol^{-1}. The main driven forces for precursor **3** and HFn were strong hydrophobic interactions with the amino acids lysine 143 (Lys. 143), alanine 144 (Ala. 144), and electrostatic interactions with glutamine 61 (Glu. 61), glutamine 147 (Glu. 147), as well as hydrogen bond interactions with lysine 53 (Lys. 53), and glutamate 140 (Glu. 140) (Fig. S12 and S13, ESI†), which indicated that the hydrogen bond between the nitrogen in the precursor **3** and the amino acid plays a major role in the formation process of HFn-PtMs. The stability of the HFn-PtM was evaluated at different pH values (pH 5.0, 6.5 and 7.2) at 37 °C for 24 h. UV/Vis measurements showed that the 450 nm absorption intensity of PtM did not change after 24 h incubation at different pH values using dialysis bags (Fig. S14, ESI†). In addition, we observed the morphology of the HFn-PtM after 24 h incubated with PBS and PBS containing 10% fetal bovine serum at 37 °C, respectively (Fig. S15, ESI†), the well-preserved spherical morphology further suggested that the HFn-PtM have good stability. After the endocytosis of HFn-PtM, HFn was biodegraded into free amino acids within the lysosomes to release the drug.[45] The specific cellular targeting and distribution of HFn-PtMs were studied by confocal laser scanning microscopy. Briefly, three different cell lines, including MCF-7 cells, CT26 cells and HFF-1cells (normal cells), were cultured with HFn-PtMs for 4 h and Hoechst 33258 with blue fluorescence was used to stain the nuclei. As shown in Fig. S16 (ESI†), MCF-7 cells and CT26 cells that overexpress TfR1 showed red fluorescence in the

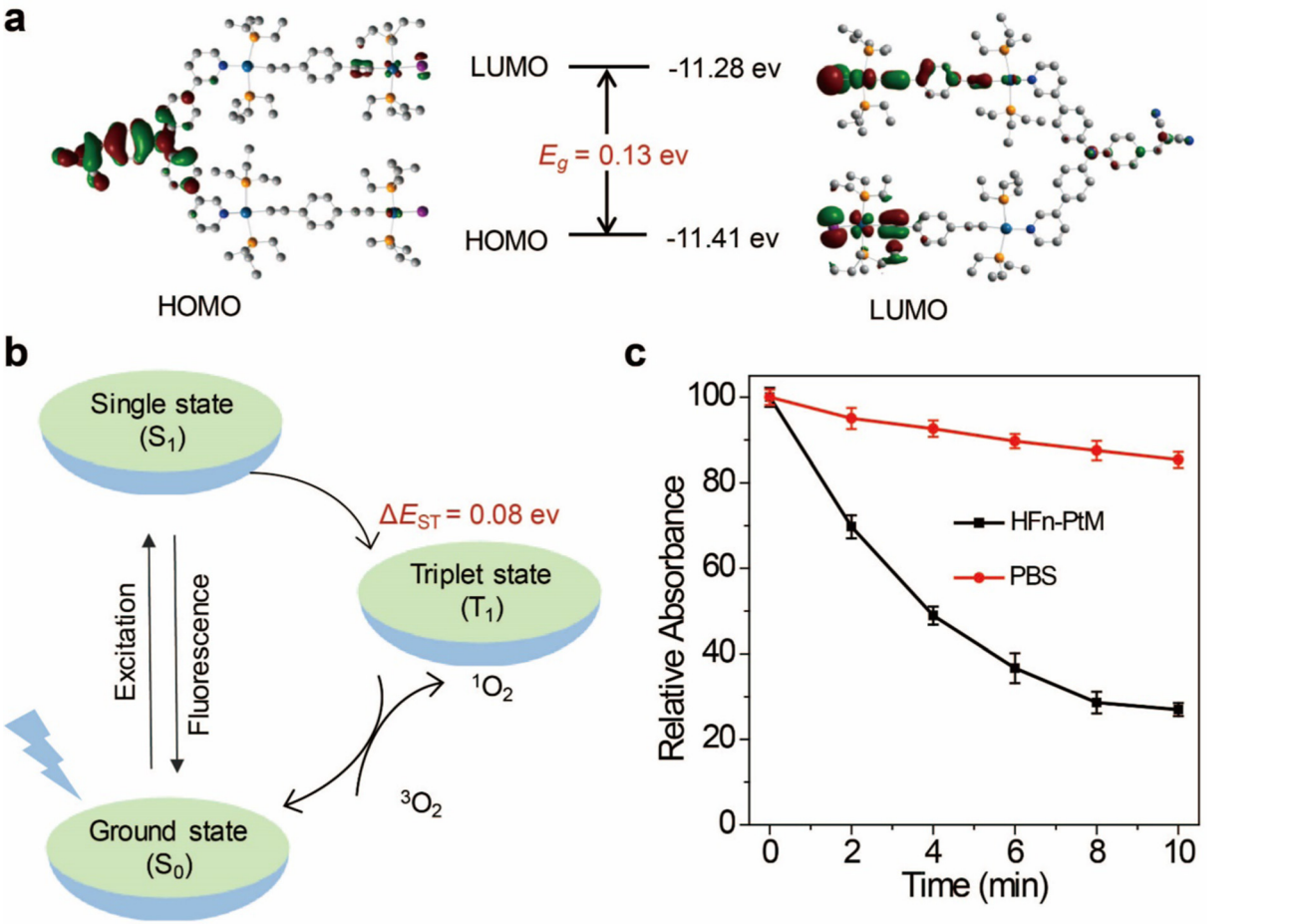

Fig. 3 Molecular calculation and photodynamic characterization in solution. (a) The optimize half complex structures of the HOMO and the LUMO at S_0 were calculated by time-dependent density functional theory (DFT) (Gaussian 09/B3LYP/LANL2DZ). (b) Simplified Jablonski diagram depicting the electron transitions of ligand 1 upon light excitation, and energy transfer from T_1 to oxygen, generating cytotoxic $^1O_2$. (c) Absorption (400 nm) response of ABDA (50 μM) upon treatment with 10 μM HFn-PtM or control under light irradiation (100 mW cm^{-2}) for 2 min, 4 min, 6 min, 8 min, and 10 min, respectively.

cytoplasm after incubation with HFn-PtMs, mainly because HFn directly targets TfR1.[46] While weak red fluorescence was observed with the HFF-1 cells, providing further support for the receptor-mediated endocytosis of HFn-PtMs. The cellular uptake of HFn-PtMs was further quantified using inductively coupled plasma mass spectrometry (ICP-MS) analysis. MCF-7 cells were incubated for 0, 5, and 15 h, respectively. As shown in Fig. S17 (ESI†), ICP-MS analysis indicated that the cellular uptake of HFn-PtMs gradually increased with increasing incubation time. Taken together, these data indicate that HFn-PtMs can be actively targeted in tumor cells.

We also investigated the singlet oxygen generation capability of the HFn-PtM. Separating the highest energy occupied molecular orbital (HOMO) and the lowest energy unoccupied molecular orbital (LUMO) distribution is of great significance for reducing ΔE_{ST}.[47] The DFT calculations were used to obtain the HOMO and the LUMO of the half complex PtM structure and precursor **3**, respectively (Fig. 3a and Fig. S18, ESI†). Obviously, the molecular orbitals of the half complex PtM structure were significantly different from those of precursor **3**. Benefiting from the introduction of Pt, the $^1O_2$ generation efficiency of metallacycles was greatly improved (Fig. 3b).[48] The $^1O_2$ sensor, 9,10-anthracenediyl bis(methylene)dimalonic acid (ABDA), was used to evaluate the $^1O_2$ generation capacity of HFn-PtMs. The absorption intensity at 400 nm of ABDA decreased after 2 min of irradiation in the presence of HFn-PtMs (Fig. S19, ESI†), confirming the photosensitizing activity of HFn-PtMs. We further investigated the absorption response of ABDA upon treatment with HFn-PtMs for 10 min under white light irradiation. As shown in Fig. 3c, HFn-PtMs exhibited an obvious decrease in absorption intensity, while only a slight decrease was observed with PBS. In addition, the intracellular $^1O_2$ generation ability of HFn-PtMs under light irradiation was examined. Dichlorofluorescein diacetate (DCF-DA) can be rapidly oxidized to fluorescent dichlorofluorescein (DCF) with green fluorescence in the presence of ROS. As shown in Fig. 4, intense green fluorescence was observed in tumor cells treated with HFn-PtMs under white light irradiation in the presence of DCF-DA. Furthermore, the green fluorescence signal of DCF was negligible under the same conditions without light irradiation.

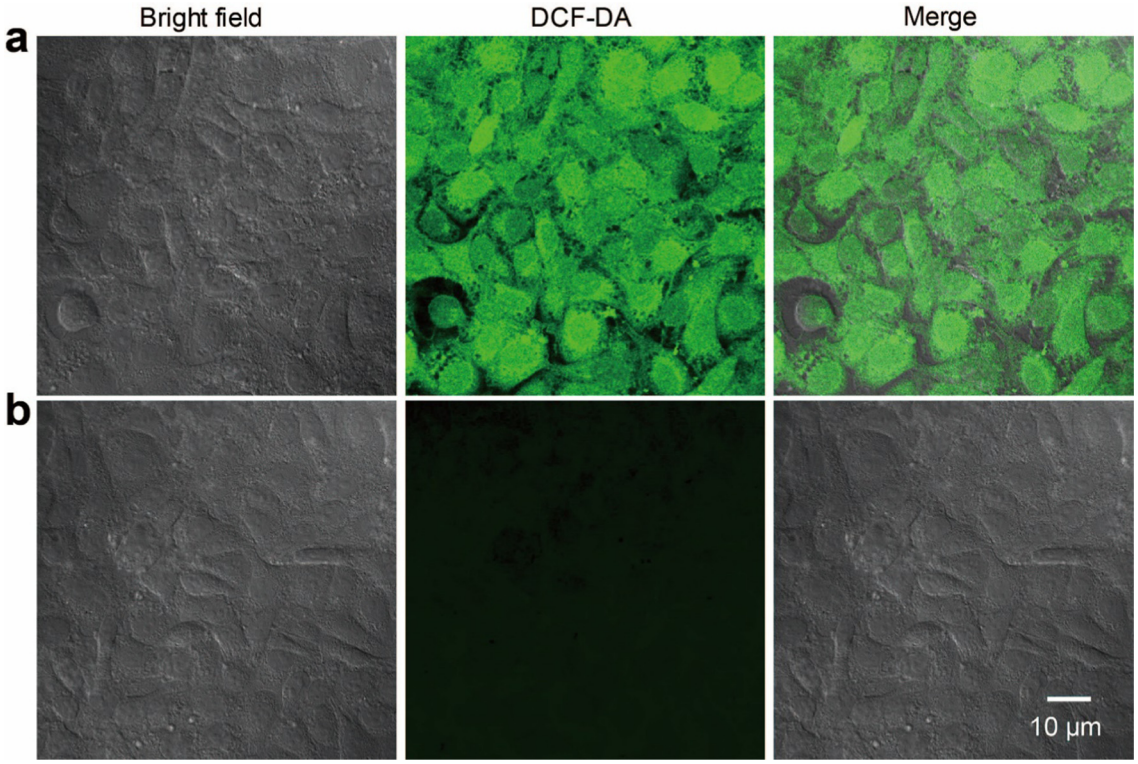

Fig. 4 Detection of intracellular ROS levels of the HFn-PtM using the DCF-DA probe (10 μM). Confocal fluorescence images exhibit MCF-7 cells were incubated (a) or not incubated (b) with 10 μM HFn-PtM, while irradiated with light (200 mW cm^{-2}) for 10 min. For DCF-DA detection, λ_{ex} was 488 nm, and λ_{em} was 505–525 nm.

These results indicated that the HFn-PtM has a good photosensitizing ability.

The cytotoxicity of HFn-PtMs was studied using the cell counting kit-8 assay to evaluate the effect of the HFn-PtM against cancer cells. As shown in Fig. 5a, the viability of CT26 cancer cells treated with HFn-PtM plus light irradiation was lower than the cells treated with only HFn-PtM, demonstrating that the chemo-photodynamic combination therapy was superior to chemotherapy alone. There was no significant cytotoxic effect on the HFF-1 cells with or without light irradiation at all tested concentrations of the HFn-PtM, mainly because hardly any HFn-PtM entered the HFF-1 cells during incubation (Fig. 5b). Moreover, after 4 h incubation with 10 μM HFn-PtM and exposure to white light irradiation (200 mW cm^{-2}, 10 min),

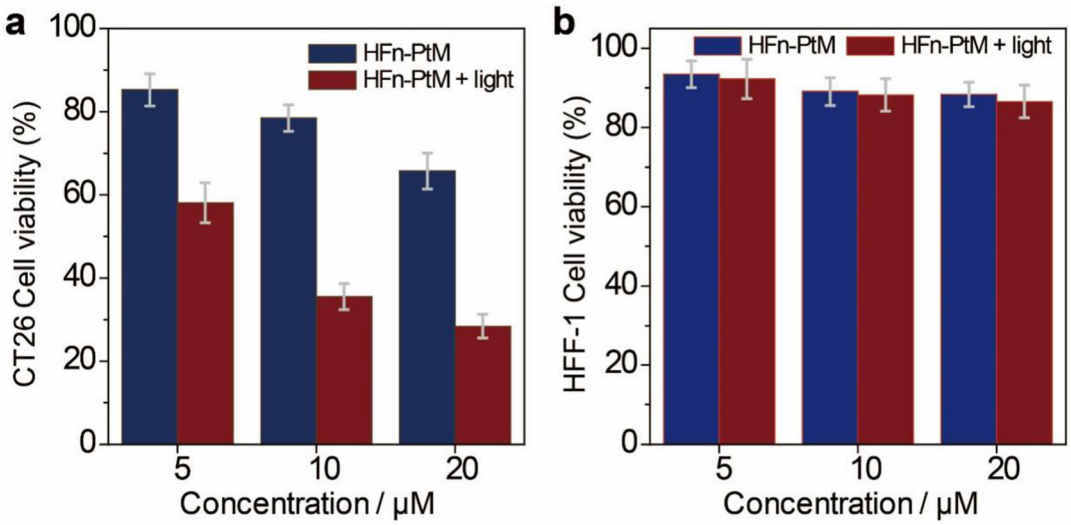

Fig. 5 Cytotoxicity of the HFn-PtM *in vitro*. Cytotoxicity of the HFn-PtM against (a) CT26 cells and (b) HFF-1 cells with or without light irradiation (200 mW cm^{-2}, 10 min) and cultured for another 24 h.

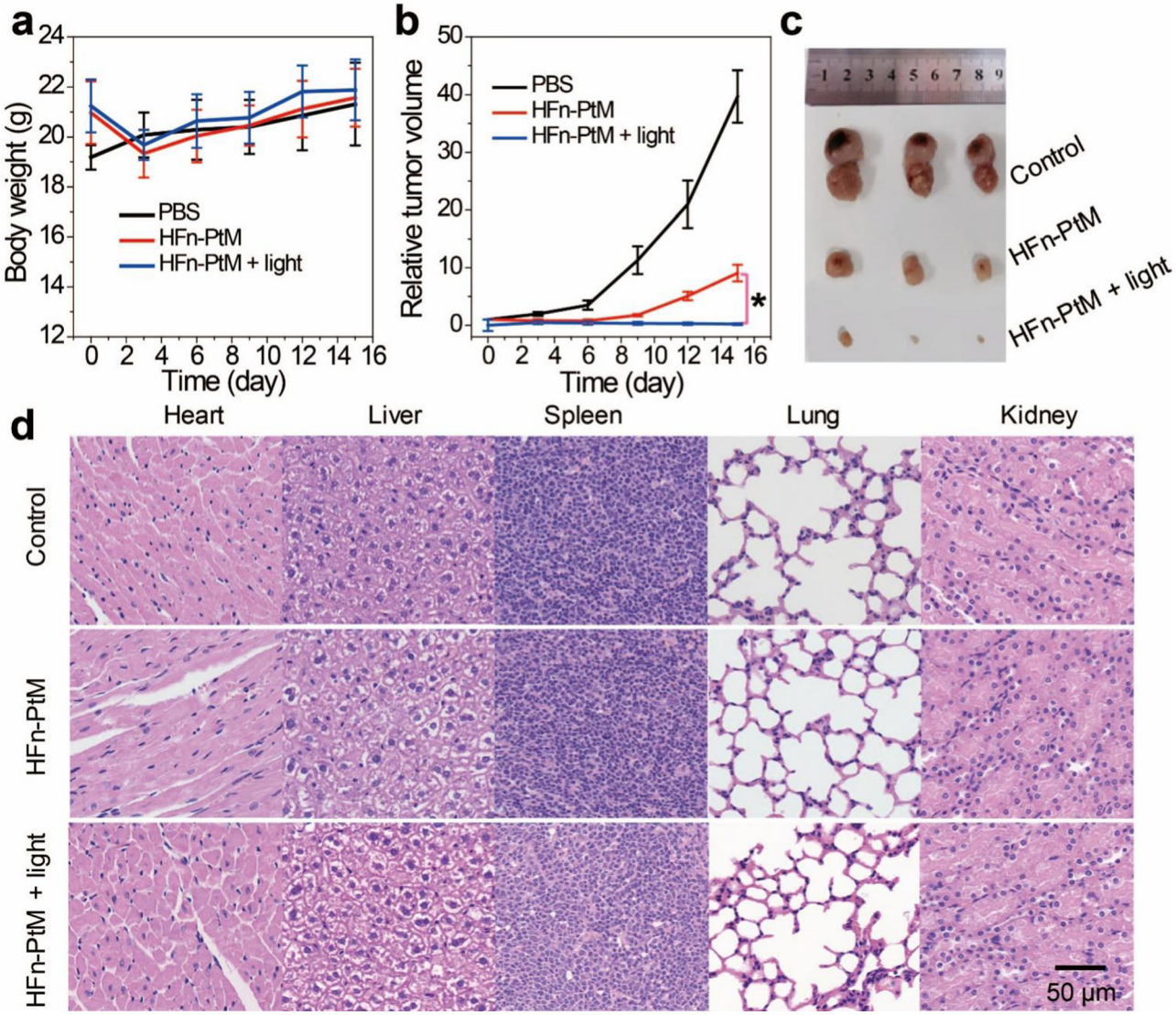

Fig. 6 The therapeutic effect was studied in CT26 tumor-bearing mice with the HFn-PtM. (a) Tumor growth inhibition curves. (b) Mice body weight change post various treatments, the mice in the irradiation groups were irradiated with white light (200 mW cm^{-2}, 10 min). (c) Photograph of tumors of each group was taken after treatment. (d) Histopathological analyses of major organs (heart, liver, spleen, lungs, and kidneys) in various groups after 15 days.

almost all CT26 cells came off the culture plate when the incubation time was extended to another 24 h (Fig. S20, ESI†). Taken together, these results indicate that the HFn-PtM has active targeting and a strong ability to kill tumor cells.

We examined the active targeting of the nanoparticles *in vivo*. The degree of fluorescence at the tumor was stronger than the surrounding fluorescence background at 24 h post-injection (Fig. S21, ESI†). This observation suggested that the HFn-PtM possesses a good active targeting ability. To examine the antitumor effect of the HFn-PtM *in vivo*, we observed the body weight and tumor volume of CT26 tumor-bearing mice after intravenous injection. Three groups of mice were injected with HFn-PtM (50 μM) (two identical treatment groups) and PBS (control group) on days 1 and 7. However, the mice in the treatment group lost weight initially, probably because of the slightly higher dose of PtM. Interestingly, there were no significant differences in body weights between the HFn-PtM treated group and the PBS control group after 15 days (Fig. 6a), suggesting the negligible systemic cytotoxicity of the HFn-PtM during the PDT. As shown in Fig. 6b, the tumors grew rapidly in the PBS-treated group but were significantly suppressed in the treatment group. There was a considerable difference in the *in vivo* antitumor efficacy observed in the treated and control groups, which was further intuitively reflected in the bright field images of mice bearing CT26 tumor post various treatments (Fig. S22, ESI†) and in the images of the tumor tissues (Fig. 6c). Additionally, the satisfactory therapeutic efficacy with no observed significant pathological changes was further confirmed *via* standard H&E staining on tissue sections after treatment. We observed no significant pathological changes in the major organs (heart, liver, spleen, lungs, and kidneys) in the treated groups compared with the PBS group, in particular,

the nephrotoxicity was very low (Fig. 6d), indicating there was low systemic toxicity during the treatment.

4. Conclusions

In summary, PtM with suitable properties for use in chemotherapy and PDT was readily prepared *via* coordination-driven self-assembly. The hydrophobic PtM molecules were encapsulated into the cavity of HFn by dissociation of the HFn and reassembly, which give HFn-PtM that could function as an active-targeting nanomedicine. Interestingly, the HFn-PtM was sufficiently stable in the delivery process under physiological conditions and could efficiently enter specific cells that overexpress TfR1. *In vitro* cytotoxicity and *in vivo* antitumor studies indicated that the HFn-PtM exhibited remarkable antitumor efficiency with negligible systemic toxicity. This work demonstrated the great potential of developing discrete metallacycles for selective therapies for cancer, thus extending the application of SCC-based materials in the field of biotechnology and biomaterials.

Author contributions

Xuehong Min, Ming Li and Wenjing Zhang contributed equally to this work. Feng Li, Yue Sun and Yi Liu designed and directed the project. Xuehong Min, Runhao Li, Zhe Zhang and Pingshan Wang prepared the metallacycle and measured the photophysical properties. Xuehong Min and Ming Li performed the *in vitro* experiments. Xuehong Min, Wenjing Zhang and Ming Li performed the *in vivo* experiments and data analysis. Xuehong Min, Feng Li, Yi Liu and Yue Sun edited and reviewed the manuscript. All authors contributed to discussions.

Conflicts of interest

There are no conflicts to declare.

Acknowledgements

This work is supported by the National Natural Science Foundation of China (No. 31771103), the CAS Emergency Project of ASF Research (KJZD-SW-L07), the Scientific Instrument Developing Project of the Chinese Academy of Sciences (No. YJKYYQ20190057), Science and Technology Plans of Tianjin (21ZYJDJC00050), and the Applied Basic Research Program of Wuhan (No. 2018060401011327). The authors are grateful to Ding Gao, Pei Zhang, and Bichao Xu of the Core Facility and Technical Support, Wuhan Institute of Virology, for technical support in TEM.

References

1 G. C. Yu, M. J. Jiang, F. H. Huang and X. Y. Chen, *Curr. Opin. Chem. Biol.*, 2020, **61**, 19–31.
2 R. Saha, A. Devaraj, S. Bhattacharyya, S. Das, E. Zangrando and P. S. Mukherjee, *J. Am. Chem. Soc.*, 2019, **141**, 8638–8645.
3 A. Ajibola Adeyemo, A. Shettar, I. A. Bhat, P. Kondaiah and P. S. Mukherjee, *Inorg. Chem.*, 2017, **56**, 608–617.
4 Y. Sun, S. Li, Z. X. Zhou, M. L. Saha, S. Datta, M. M. Zhang, X. Z. Yan, D. M. Tian, H. Wang, L. Wang, X. P. Li, M. H. Liu, H. B. Li and P. J. Stang, *J. Am. Chem. Soc.*, 2018, **140**, 3257–3263.
5 L. He, L. X. Cai, M. H. Li, G. L. Zhang, L. P. Zhou, T. Chen, M. J. Lin and Q. F. Sun, *Chem. Sci.*, 2020, **11**, 7940–7949.
6 H. Fan, K. Li, T. Tu, X. Zhu, L. Zhang and M. Liu, *Angew. Chem., Int. Ed.*, 2022, **61**, 202200727–202200732.
7 R. H. Li, X. Y. Feng, J. Zhou, F. Yi, Z. Q. Zhou, D. Men and Y. Sun, *Inorg. Chem.*, 2020, **60**, 431–437.
8 Y. Sun, F. Ding, Z. Chen, R. Zhang, C. Li, Y. Xu, Y. Zhang, R. Ni, X. Li, G. Yang, Y. Sun and P. J. Stang, *Proc. Natl. Acad. Sci. U. S. A.*, 2019, **116**, 16729–16735.
9 Y. Yao, R. Zhao, Y. Shi, Y. Cai, J. Chen, S. Sun, W. Zhang and R. Tang, *Chem. Commun.*, 2018, **54**, 8068–8071.
10 Y. Yin, Z. Chen, R. H. Li, F. Yi, X. C. Liang, S. Q. Cheng, K. Wang, Y. Sun and Y. Liu, *Inorg. Chem.*, 2022, **61**, 2883–2891.
11 G. C. Yu, B. Zhu, L. Shao, J. Zhou, M. L. Saha, B. Shi, Z. Zhang, T. Hong, S. Li, X. Y. Chen and P. J. Stang, *Proc. Natl. Acad. Sci. U. S. A.*, 2019, **116**, 6618–6623.
12 W. J. Li, Z. Hu, L. Xu, X. Q. Wang, W. Wang, G. Q. Yin, D. Y. Zhang, Z. Sun, X. Li, H. Sun and H. B. Yang, *J. Am. Chem. Soc.*, 2020, **142**, 16748–16756.
13 Y. Wang, R. Tang, D. Wang, J. Wang, Y. Huang, Y. Ding, B. Lu, Y. Sun, P. J. Stang and Y. Yao, *Inorg. Chem.*, 2021, **60**, 7627–7631.
14 X. Wang, Q. Su, Z. Zhang, J. Yang, Y. Zhang and M. Zhang, *Chem. Commun.*, 2020, **56**, 8460–8463.
15 Y. Sun, F. Ding, Z. Zhou, C. Li, M. Pu, Y. Xu, Y. Zhan, X. Lu, H. Li, G. Yang, Y. Sun and P. J. Stang, *Proc. Natl. Acad. Sci. U. S. A.*, 2019, **116**, 1968–1973.
16 G. C. Yu, M. M. Zhang, M. L. Saha, Z. Mao, J. Chen, Y. Yao, Z. Zhou, Y. Liu, C. Gao, F. Huang, X. Y. Chen and P. J. Stang, *J. Am. Chem. Soc.*, 2017, **139**, 15940–15949.
17 J. Zhou, G. Yu, J. Yang, B. Shi, B. Ye, M. Wang, F. Huang and P. J. Stang, *Chem. Mater.*, 2020, **32**, 4564–4573.
18 G. C. Yu, T. R. Cook, Y. Li, X. Yan, D. Wu, L. Shao, J. Shen, G. Tang, F. Huang, X. Y. Chen and P. J. Stang, *Proc. Natl. Acad. Sci. U. S. A.*, 2016, **113**, 13720–13725.
19 Y. Sun, C. Chen, J. Liu and P. J. Stang, *Chem. Soc. Rev.*, 2020, **49**, 3889–3919.
20 W. Tuo, Y. Xu, Y. Fan, J. Li, M. Qiu, X. Xiong, X. Li and Y. Sun, *Coordin. Chem. Rev.*, 2021, **443**, 214017–214030.
21 N. Bertrand, J. Wu, X. Xu, N. Kamaly and O. C. Farokhzad, *Adv. Drug Delivery Rev.*, 2014, **66**, 2–25.
22 J. Yoo, C. Park, G. Yi, D. Lee and H. Koo, *Cancers*, 2019, **11**, 640–652.
23 K. Fan, L. Gao and X. Yan, *Wiley Interdiscip. Rev.: Nanomed. Nanobiotechnol.*, 2013, **5**, 287–298.
24 F. Nasrollahi, B. Sana, D. Paramelle, S. Ahadian, A. Khademhosseini and S. Lim, *Adv. Ther.*, 2020, **3**, 1900183.
25 X. Lin, J. Xie, L. Zhu, S. Lee, G. Niu, Y. Ma, K. Kim and X. Chen, *Angew. Chem.*, 2011, **50**, 1569–1572.

26 C. Cao, X. Wang, Y. Cai, L. Sun, L. Tian, H. Wu, X. He, H. Lei, W. Liu, G. Chen, R. Zhu and Y. Pan, *Adv. Mater.*, 2014, **26**, 2566–2571.
27 B. Zhang, G. Tang, J. He, X. Yan and K. Fan, *Adv. Drug Delivery Rev.*, 2021, 113892–113908.
28 Y. Shen, X. Li, D. Dong, B. Zhang, Y. Xue and P. Shang, *Am. J. Cancer Res.*, 2018, **8**, 916–931.
29 D. E. Dolmans, D. Fukumura and R. K. Jain, *Nat. Rev. Cancer*, 2003, **3**, 380–387.
30 X. Qin, M. Zhang, Z. Zhao, Q. Du, Q. Li, Y. Jiang, F. Xue and Y. Luan, *Acta Biomater.*, 2022, **147**, 366–376.
31 M. Zhang, X. Qin, W. Xu, Y. Wang, Y. Song, S. Garg and Y. Luan, *J. Colloid Interface Sci.*, 2021, **594**, 493–501.
32 J. L. Yang, J. Dai, Q. Wang, Y. Cheng, J. Guo, Z. Zhao, Y. Hong, X. D. Lou and F. Xia, *Angew. Chem., Int. Ed.*, 2020, **59**, 20405–20410.
33 X. D. Wang, J. Dai, X. Wang, Q. Hu, K. X. Huang, Z. J. Zhao, X. D. Lou and F. Xia, *Talanta*, 2019, **202**, 591–599.
34 J. Li, Y. Zhang, P. Wang, L. Yu, J. An, G. Deng, Y. Sun and J. Seung Kim, *Coordin. Chem. Rev.*, 2021, **427**, 213559–213579.
35 X. Min, F. Yi, X. L. Han, M. Li, Q. Gao, X. Liang, Z. Chen, Y. Sun and Y. Liu, *Chem. Eng. J.*, 2022, **432**, 134327–134334.
36 X. Q. Yi, J. Dai, Y. Han, M. Xu, X. Zhang, S. Zhen, Z. Zhao, X. D. Lou and F. Xia, *Commun. Biol.*, 2018, **1**, 202–224.
37 R. Li, L. Shan, Y. Yao, F. Peng, S. Jiang, D. Yang, G. Ling and P. Zhang, *Drug Delivery Transl. Res.*, 2021, **11**, 1133–1143.
38 Z. Xie, T. Fan, J. An, W. Choi, Y. Duo, Y. Ge, B. Zhang, G. Nie, N. Xie, T. Zheng, Y. Chen, H. Zhang and J. S. Kim, *Chem. Soc. Rev.*, 2020, **49**, 8065–8087.
39 G. Li, X. Zhang, W. Zhao, W. Zhao, F. Li, K. Xiao, Q. Yu, S. Liu and Q. Zhao, *ACS Appl. Mater. Interfaces*, 2020, **12**, 20180–20190.
40 Y. Gao, G. Feng, T. Jiang, C. Goh, L. Ng, B. Liu, B. Li, L. Yang, J. Hua and H. Tian, *Adv. Funct. Mater.*, 2015, **25**, 2857–2866.
41 X. Liu, Y. Qin, J. Zhu, X. Zhao, T. Cheng, Y. Jiang, H. Sun and L. Xu, *Chin. Chem. Lett.*, 2021, **32**, 1537–1540.
42 X. H. Min, T. Fang, L. L. Li, C. Li, Z. P. Zhang, X. E. Zhang and F. Li, *Nanoscale*, 2020, **12**, 2340–2344.
43 X. H. Min, J. Zhang, R. H. Li, F. F. Xia, S. Q. Cheng, M. Li, W. W. Zhu, W. Zhou, F. Li and Y. Sun, *ACS Appl. Mater. Interfaces*, 2021, **13**, 17372–17379.
44 B. Jiang, X. Chen, G. Sun, X. Chen, Y. Yin, Y. Jin, Q. Mi, L. Ma, Y. Yang and X. Yan, *Nano Today*, 2020, **35**, 100948.
45 L. Li, C. J. Fang, J. C. Ryan, E. C. Niemi, J. A. Lebrón, P. J. Björkman, H. Arase, F. M. Torti, S. V. Torti, M. C. Nakamura and W. E. Seaman, *Proc. Natl. Acad. Sci. U. S. A.*, 2010, **107**, 3505–3510.
46 K. Fan, C. Cao, Y. Pan, D. Lu, D. Yang, J. Feng, L. Song, M. Liang and X. Yan, *Nat. Nanotechnol.*, 2012, **7**, 459–464.
47 F. Hu, S. Xu and B. Liu, *Adv. Mater.*, 2018, **30**, 1801350–1801378.
48 Z. Guo, Y. Zou, H. He, J. Rao, S. Ji, X. Cui, H. Ke, Y. Deng, H. Yang, C. Chen, Y. Zhao and H. Chen, *Adv. Mater.*, 2016, **28**, 10155–10164.